Energy loss by channeled electrons: a quantitative study on transition metal oxides

Running tittle: Quantitative Site-specific EELS using channeling

Kazuyoshi Tatsumi[*,1)], Shunsuke Muto[1)], and Ján Rusz[2)]

This research was performed primarily at Nagoya University.

1) Department of Materials, Physics and Energy Engineering, Nagoya University, Chikusa, Nagoya, Aichi Pref. 464-8603, Japan

2) Department of Physics and Astronomy, Uppsala University, Box 516, SE-75120 Uppsala, Sweden

*: Author to whom all correspondence should be addressed

TEL: +81-52-789-5135, FAX: +81-52-789-5137, E-mail: k-tatsumi@nucl.nagoya-u.ac.jp

Abstract

It has been known that electron energy-loss spectroscopy (EELS) attached to current transmission electron microscopy (TEM) can probe not only element-selective chemical information, but also site-selective information that depends on the position that a specific element occupies in a crystal lattice. The latter information is exploited by utilizing the Bloch waves symmetry in the crystal, which changes with its orientation with respect to the incident electron wave (electron channeling). We demonstrate the orientation dependence of the cross-section of the electron energy-loss near-edge structure (ELNES) for particular crystalline sites of spinel ferrites, by quantitatively taking into account the dynamical diffraction effects with a large number of the diffracted beams. The theoretical results are well consistent with a set of experiments in which the transition metal sites in spinel crystal structures are selectively excited. A new measurement scheme for site-selective EELS using a 2D position sensitive detector is proposed, validated by theoretical predictions and trial experiments.

INTRODUCTION

In electron energy-loss spectroscopy (EELS) associated with transmission electron microscopy (TEM) on a crystalline material, the incident or outgoing fast electrons in specific crystal orientations can enhance particular site- or orbital-selective electronic transitions, revealing rich information on the atomic and electronic structures of the crystal. One example is the electron channeling effect on EELS: when the orientation of the probe electron beam deviates slightly from the exact Bragg condition, a Bloch state having either odd or even symmetry with respect to the corresponding reflecting Bragg planes will be preferentially excited, resulting in the preferential localization of electron propagation on a particular set of atomic columns or planes. Thus, the channeled electron selectively enhances the electron energy-loss near-edge structures (ELNES) from atom sites in these columns/planes. The experimental setup was called energy loss by channeled electron (ELCE) (Krivanek et al., 1982) or high angular resolution electron channeling electron spectroscopy (HARECES) (Zaluzec, 2005).

ELCE has been less frequently used compared with its counterpart using fluorescent X-rays, a technique known as ‘Atom Location by CHanneling Enhanced MIcro-analysis (ALCHEMI) (Spence & Taftø, 1983) or, more generally, High Angular Resolution Electron Channeled X-ray Spectroscopy (HARECXS) (Matsumura et al., 1999), partly because ELCE depends on the orientations of both the incoming and outgoing electron beams into/from the

thin film sample, which makes the experimental setup and the interpretation of the results more complicated: in the pioneering work by Taftø and Krivanek (Taftø_& Krivanek, 1982*a* 1982*b*), the detector was located so as to allow the outgoing beam to satisfy the same boundary conditions as the incident beam, while Taftø (Taftø, 1987) then considered several combinations of the boundary conditions for the incident/scattered beams to confirm the localization effect of electron transition. Meanwhile, Batson (Batson, 1993) created odd/even symmetry-selectable excitations under a two-beam channeling condition, elaborating the geometrical configurations of incoming and outgoing (inelastically scattered) wavefunctions with different symmetries, and exploited rich information on the diamond conduction band edge. The above discussion on ELCE is only qualitative; more general formulations of the scattering matrix elements have been required for a more quantitative discussion.

In the electron inelastic scattering theory including the dynamical diffraction effects on EELS, the double differential cross-section (DDCS) of ELNES was formulated using the distorted-wave Born approximation (DWBA) (Maslen & Rossouw, 1984; Saldin,1987; Weickenmeier & Kohl, 1989; Schattschneider et al., 1996a), where the incoming and outgoing fast electrons were taken into account using the direct products between the fast-electron waves and scatterer waves for the initial and final states of the system. This approach was used to calculate theoretical energy-filtered diffraction patterns (Schattschneider et al., 1996b), electron channeling EELS (Weickenmeier & Kohl, 1989;

Rossouw & Maslen, 1984b; Schattschneider et al., 2001), dipole-forbidden transitions (Schattschneider et al., 2001), and electron magnetic circular dichroism (EMCD) (Schattschneider et al., 2006) by the interference between the Bloch waves of the fast electron being inelastically scattered. We analytically calculated the electron channeling effects on EELS, where the incoming and outgoing fast electrons were treated within the two-beam approximation based on DDCS formalism, and the derived formula provided a good qualitative explanation for experimentally observed electron channeling effects (Tatsumi & Muto, 2009).

The purpose of this study is to establish a theoretical formulation accurate enough to predict ELCE results, taking into account the many-beam dynamical scattering effect, on the basis of the ELNES cross-section calculation developed by Rusz *et al*. (Rusz et al., 2007, 2013). Having investigated the optimum condition of the original site-selective EELS scheme in ref. (Taftø & Krivanek, 1982*a*), we propose a detector-position-sensitive measurement for ELCE. A similar simulation code was developed by Allen and his coworkers (Oxley & Allen, 2003), implementing fast calculation methods for both fluorescent X-ray and EELS cross-sections with parameterized atomic scattering factors. In this code, however, the EELS detector entrance aperture was limited to be cylindrically symmetric with respect to the incident direction, which is not applicable to the general geometries used in ELCE experiments. Quantitative comparisons between ELCE experiments and theory have been

done for the transition metal $L_{2,3}$ ELNES of $NiFe_2O_4$ (Tatsumi et al., 2010) and O-*K* of TiO_2 in refs. (Nelhiebel et al., 2000; Schattschneider et al., 2001), where the different symmetry orbitals at the O site were selectively probed, and for the O-*K*/Ni $L_{2,3}$ intensity ratio of NiO in ref. (Hetaba et al., 2011, 2012). Using ELCE it was predicted for Fe_3O_4 that EMCD signals of nonequivalent sublattices can be separated (Calmels & Rusz, 2011). This was confirmed in a recent experiment on $NiFe_2O_4$ (Wang et al, 2013). The present formulation covers general geometrical conditions for ELCE, which will contribute not only to quantitative ELCE but also to a new scheme for more robust site-specific electronic structure analysis in the future.

MATERIALS AND METHODS

General formulation

In the present study, we applied the numerical calculation code developed by Rusz (Rusz et al., 2013) to calculate the electron channeling effects on EELS. Prior to investigating its applicability to electron channeling EELS, we should briefly describe the ELNES cross-section formulation on which the code is based, highlighting the atom-site dependent term in the formula (Schattschneider et al., 1996a).

Within the first-order Born approximation, the DDCS is proportional to the following quantity (Schattschneider, 1986):

$$\frac{\partial^2\sigma}{\partial E\partial\Omega} \propto \frac{S(\boldsymbol{q},E)}{q^4}, \qquad (1),$$

where

$$S(\boldsymbol{q},E)=\sum_{i,f}|<i\,|\,e^{i\boldsymbol{qr}}\,|\,f>|^2\;\delta(E_f-E_i-E). \qquad (2)$$

$<i|$ and $<f|$ are the initial and final many-electron states in the material, and E is the fast electron's energy loss. Eq. (1) is correct only if the fast electron before and after the inelastic scattering can be described as single plane waves with their wave numbers $\boldsymbol{k}_i$ and $\boldsymbol{k}_f$ related by the momentum transfer $\hbar\boldsymbol{q} = \hbar(\boldsymbol{k}_f - \boldsymbol{k}_i)$. We set an acceleration voltage of 200 kV for the incident electron beam, as in our experiment. A crystalline sample essentially diffracts an incident electron into a number of plane waves, and the associated momentum transfer vectors modify DDCS as introducing the cross terms between the vectors (Kohl & Rose, 1985):

$$S(\boldsymbol{q},\boldsymbol{q}',E)=\sum_{i,f}<i\,|\,e^{i\boldsymbol{qr}}\,|\,f><f\,|\,e^{-i\boldsymbol{q}'\boldsymbol{r}}\,|\,i>\delta(E_f-E_i-E)\,, \qquad (3)$$

where $\boldsymbol{q}=\boldsymbol{k}^{(l)}-\boldsymbol{k}^{(j)}+\boldsymbol{h}-\boldsymbol{g}$, $\boldsymbol{q}'=\boldsymbol{k}^{(l')}-\boldsymbol{k}^{(j')}+\boldsymbol{h}'-\boldsymbol{g}'$, and $\boldsymbol{k}^{(i)}$ are wave number vectors excited on the i-th branch (dispersion surface) of the Bloch states, with the superscripts j and j' (l and l') for the incoming (outgoing) waves. $\boldsymbol{g}$ and $\boldsymbol{g}'$ ($\boldsymbol{h}$ and $\boldsymbol{h}'$) are reciprocal lattice vectors of operating incoming (outgoing) waves, respectively. $S(\boldsymbol{q},\boldsymbol{q}',E)$, which is called a mixed dynamic form factor (MDFF), depends on the electronic structure of the crystal. Summation over the operating diffraction spots and $\boldsymbol{q}$ associated with their possible scattering paths for the atoms at a specific site within the unit cell simulates the atom site-selective DDCS for a specimen with thickness t (Schattschneider et al., 1996a):

$$\frac{\partial^2\sigma_{site}}{\partial E\partial\Omega}\propto\sum_{u\subset site}^{unitcell}\sum_{jj'}\sum_{gg'}\sum_{ll'}\sum_{hh'}T_{jj'll'}(t)\,Y_{ghg'h'}^{jlj'l'}\,\frac{S_u(\boldsymbol{q},\boldsymbol{q}',E)}{\boldsymbol{q}^2\boldsymbol{q}'^2}\,e^{i(\boldsymbol{q}-\boldsymbol{q}')\boldsymbol{u}},$$

$$T_{jj'll'} = \frac{\cosh(\delta\eta\frac{t}{2})\sin(\Delta\frac{t}{2}) + i\sinh(\delta\eta\frac{t}{2})\cos(\Delta\frac{t}{2})}{\Delta\frac{t}{2} + i\delta\eta\frac{t}{2}},$$

$$Y^{jlj'l'}_{ghg'h'} = C_0^{(j)*}C_g^{(j)}D_0^{(l)}D_h^{(l)*}C_0^{(j')}C_{g'}^{(j')*}D_0^{(l')*}D_{h'}^{(l')}$$

$$\Delta = \gamma^{(j)} - \gamma^{(j')} - (\gamma^{(l)} - \gamma^{(l')}), \delta\eta = \eta^{(j)} - \eta^{(j')} - (\eta^{(l)} - \eta^{(l')}) \quad (4)$$

where $C_g^{(j)}$ ($D_h^{(l)}$) is the Fourier coefficient associated with the elastic scattering vector $\boldsymbol{g}$ ($\boldsymbol{h}$) for the j-th (l-th) branch of the incoming (outgoing) wave. $T_{jj'll'}$ is a thickness function that describes the specimen thickness effect and the nominal absorption phenomenologically, with the real (γ) and imaginary (η) parts of the eigenvalues of the Bloch states introduced (Spence & Zuo, 1992). $\boldsymbol{u}$ is the atom position in the unit cell, and the term $\sum_{u}^{unitcell} e^{i(\boldsymbol{q}-\boldsymbol{q}')\boldsymbol{u}}$ acts as a structure factor determining the atomic site-selectivity.

We constructed the Fourier coefficients of the real part of the crystal potential, V_g, using the formula from ref. (Weickenmeier & Kohl, 1991); those of the imaginary part, V_g', were phenomenologically set to V_g' = 0.1 V_g, which provided reasonable fit with the experiments within the experimental error. The total cross-section at a specific atomic site, σ_{site}, is obtained by integrating $\partial^2\sigma_{site}/\partial E\partial\Omega$ over the solid angles subtended by the experimental convergent and collection angles, ϕ_{conv} and ϕ_{col}, and over the energy loss E from the edge threshold E_{th} to E_{th} + 15 eV, where the ELNES mainly appears. MDFF can be reduced to the electric dipole approximation for small q and q' so as to minimize computational cost (Kohl & Rose, 1985):

$$S_u(\boldsymbol{q},\boldsymbol{q}',E) \approx Const.\boldsymbol{q}\cdot\boldsymbol{q}'\delta(E_f - E_i - E). \quad (5)$$

We confirm that the typical number of diffracted beams large enough to reach

well-converged results is around 80 and 25, respectively, for solving the secular equations of the Bloch states and for the summation of Eq. (4).

Experiments

The calculated site-specific cross-sections of Fe $L_{2,3}$ were compared with the experimental results for three types of spinel ferrites, *viz*. $NiFe_2O_4$, $CoFe_2O_4$ and $MnFe_2O_4$, where two kinds of Fe sites were coordinated by 4 (tetrahedral (tet) site) and 6 (octahedral (oct) site) O atoms and lying on alternately stacking planes with {400} periodicity. We measured the transition metal $L_{2,3}$ spectra with different excitation errors of $\boldsymbol{g}$ = 400, which resulted from consecutive tilting of the incident beam with the set-up in Fig. 1 inset. This means that both incoming and outgoing beams are tilted synchronously, being equivalent to tilting the crystal with respect to the incoming beam. A dimensionless parameter, $w_g=s_g\xi_g$, where s_g and ξ_g are the excitation error of the incident beam and extinction distance for a Bragg spot $\boldsymbol{g}$, respectively, is hereafter used to represent the tilting. The beam convergence and the size and position of the detector aperture used in the experiments are listed in Table 1. Details of the experimental setup and data processing procedures were identical to those in ref. (Tatsumi et al, 2010) for $NiFe_2O_4$.

Another measurement scheme, detector-position-sensitive ELCE was attempted on Mn-$L_{2,3}$ ELNES of Mn_3O_4, where Mn^{2+} and Mn^{3+} occupy the tetrahedral and octahedral sites in the

spinel structure, respectively. The crystal orientation was set on the symmetric $n00$ systematic row excitation condition ($w_{400} = w_{\bar{4}00} < 0$) and the convergence semiangle of the incident beam was 4.9 mrad.

A JEOL-2100 TEM (an acceleration voltage of 200 kV) and a Gatan Enfina 1000 EELS were used for both of the ELCE measurements.

RESULTS AND DISCUSSION

Check of theoretical calculation: Dipole approximation

In order to validate the dipole approximation in Eq. (5), we compared the incident beam orientation dependence of σ_{site} with and without the approximation for the example in our previous paper: Fe $L_{2,3}$ of two kinds of Fe sites in $NiFe_2O_4$ spinel. The full MDFF calculation was done by the first-principles APW+lo method (Blaha et al, 2001), in which no multiplet splitting was taken into consideration (Nesvizhskii et al., 2001) Figure 1 shows $\sigma_{tet}/(\sigma_{tet} + \sigma_{oct})$ as an indicator of the EELS site-selectivity due to electron channeling. There seems to be no significant deviation between the electric dipole approximation and the full calculation for the further discussion and comparison between theory and experiment.

Check of theoretical calculation: Two-beam case

Within the two-beam approximation, where the only one Bragg reflection is strongly excited, the Bloch coefficients and eigenvalues are analytically given by (Hirsch et al., 1977)

$$
\begin{aligned}
&C_0^{(1)} = C_g^{(2)} = \cos\frac{\beta}{2}, C_0^{(2)} = -C_g^{(1)} = \sin\frac{\beta}{2}, w_g = s_g\xi_g = \cot\beta \\
&\gamma^{(1)} = 2\pi\left(w_g - \sqrt{{w_g}^2+1}\right)/2\xi_g, \gamma^{(2)} = 2\pi\left(w_g + \sqrt{{w_g}^2+1}\right)/2\xi_g \\
&\eta^{(1)} = 2\pi\left(1 - \frac{1}{\sqrt{1+{w_g}^2}}\right)/20\xi_g, \eta^{(2)} = 2\pi\left(1 + \frac{1}{\sqrt{1+{w_g}^2}}\right)/20\xi_g
\end{aligned}
\qquad (6).
$$

The phenomenological absorption can be taken into account by introducing the complex extinction distance with the imaginary part ξ_g'. In Eq. (6), $\xi_g' = 10\xi_g$, which is equivalent to the two-beam case for the numerical calculation with $V_g' = 0.1V_g$ in the previous section. For the experimental setup shown in the inset of Fig. 1, $D_g^{(i)} = C_g^{(i)}$ since the detector is located off-axis with respect to the transmitted beam parallel to the Kikuchi line, which guarantees the same boundary condition to apply to the incoming and outgoing waves. By substituting Eq. (6) into Eq. (4), the site-dependent term of EELS is derived analytically. For an arbitrary crystal with atomic planes containing sites A and B, stacking alternately as ABABAB… with a periodicity of $1/g$,

$$
\begin{aligned}
\sigma_A - \sigma_B \propto &\left(\cos^7\frac{\beta}{2}\sin\frac{\beta}{2} + \cos^5\frac{\beta}{2}\sin^3\frac{\beta}{2} - \cos^3\frac{\beta}{2}\sin^5\frac{\beta}{2} - \cos\frac{\beta}{2}\sin^7\frac{\beta}{2}\right) \\
&\times\left[\frac{\boldsymbol{d}\cdot(\boldsymbol{d}+\boldsymbol{g})}{\boldsymbol{d}^2(\boldsymbol{d}+\boldsymbol{g})^2} + \frac{\boldsymbol{d}\cdot(\boldsymbol{d}-\boldsymbol{g})}{\boldsymbol{d}^2(\boldsymbol{d}-\boldsymbol{g})^2}\right]\times\left[\pi\sqrt{{w_g}^2+1}t - \cos\left(\frac{\pi\sqrt{{w_g}^2+1}t}{\xi_g}\right)\sin\left(\frac{\pi\sqrt{{w_g}^2+1}t}{\xi_g}\right)\right],
\end{aligned}
\qquad (7)
$$

using $\boldsymbol{d}$ and $\boldsymbol{g}$ as defined in the inset of Fig. 1. For simplicity, the absorption effect is not included in Eq. (7). To examine Al-*K* ELNES of $NiAl_2O_4$ spinel, which hypothetically has the

same number of Al atoms per unit cell at the tetrahedral and octahedral sites, we set $\boldsymbol{g}$ = 400. $(\sigma_{tet}-\sigma_{oct})/(\sigma_{tet}+\sigma_{oct})$ values calculated by the analytical formula and by numerical calculation (Rusz et al., 2013) are compared in Fig. 2; the absorption effect was included in Fig. 2(b). The two approaches are consistent with each other, confirming the validity of the present numerical calculations. Note that when the absorption was taken into account, the component from the tetrahedral site dominated even at the exact Bragg condition (w_g = 0). This asymmetric behavior is the result of anomalous absorption, where the electron wave concentrated near the planes with higher density is absorbed more strongly (Spence & Zuo, 1992).

Comparison between experiments and theoretical calculations of intrinsic site-selective ELCE in transition metal ferrites

Neglecting the insignificant energy dependence of electron channeling effects over the ELNES, the total intensity of Fe $L_{2,3}$, $I(E)$ of the spinel ferrites, can be expressed as

$$I(E) \propto N_{tet}\sigma_{tet}I_{tet}(E) + N_{oct}\sigma_{oct}I_{oct}(E) = w_{tet}I_{tet}(E) + w_{oct}I_{oct}(E), \qquad (8)$$

where $I_{tet}(E)$ and $I_{oct}(E)$ are the pure site-specific spectra normalized per atom. N_{oct} and N_{tet} are the number of Fe atoms occupying the octahedral and tetrahedral sites, respectively. Thus, w_{tet} and w_{oct} stand for the weight of each site-specific spectral component of the measured spectrum. From the experimental spectral data, we resolved ($I_{tet}(E)$, $I_{oct}(E)$) and (w_{tet}, w_{oct}) by

a multivariate curve resolution (MCR) technique (Yamamoto at al., 2007; Tatsumi et al., 2009, 2010).

Figure 3-a shows the fraction of the spectral intensity from the tetrahedral site in the total spectral intensity, which is related to the site occupancy ratio of iron, N_{oct}/N_{tet}, and the total cross-section of each site by

$$\frac{w_{tet}}{w_{tet}+w_{oct}} = \frac{\sigma_{tet}N_{tet}}{\sigma_{tet}N_{tet}+\sigma_{oct}N_{oct}} = \frac{\sigma_{tet}}{\sigma_{tet}+\sigma_{oct}N_{oct}/N_{tet}} . \quad (9)$$

In $CoFe_2O_4$ and $NiFe_2O_4$, $N_{oct}/N_{tet} \approx 1.0$, whereas for $MnFe_2O_4$, various occupancies from normal spinel ($N_{tet} = 0$) to inverse spinel ($N_{oct}/N_{tet} = 1.0$) have been reported experimentally, depending on the synthesis conditions (Holgersson, 1927; Denecke et al., 1992; Antic et al., 2004). We found that the composition $(Mn_{0.5}Fe_{0.5})^{tet}(Fe_{1.5}Mn_{0.5})^{oct}O_4$ represented a rough agreement between calculated and experimental profiles in $MnFe_2O_4$. A new measure, $(w_{tet}/w_{oct})^* = (\sigma_{tet}/\sigma_{oct})^*$ (* implies normalization by the average value of the data, which eliminates the occupancy ratio, N_{oct}/N_{tet}, from the data points), is thus introduced for a simpler comparison between theory and experiment, as shown in Fig. 3-b. The experimental and theoretical profiles are generally consistent, though discrepancies for $w_{400} > 2$ in $NiFe_2O_4$ seem to be exaggerated by the present standardization.

Optimum experimental parameters for site-selective ELCE experiment

The results shown in Fig. 4 can provide a guiding principle for the optimum measurement conditions (incident beam convergence, detector position and its collection angle) in site-selective ELCE experiments, because it is statistically desirable to maximize the change in the signal fraction of each component with the diffraction conditions, in order to correctly resolve the pure components through multivariate analysis (Yamamoto et al., 2007). Figure 4 shows the calculated Fe $L_{2,3}$ signal fractions of the tetrahedral site in $CoFe_2O_4$, $\sigma_{tet}/(\sigma_{tet}+\sigma_{oct})$, as functions of the incident beam orientation (w_{400}), changing the convergent semi-angle ϕ_{conv} of the incident beam, detector collection semi-angle ϕ_{col}, and collection aperture shift d between five different values. The direction of the off-axis shift was parallel to the Kikuchi lines of $\boldsymbol{g}$ = 400, as in Fig. 1. It is seen from Figs. 4-a and 4-b that ϕ_{col} and ϕ_{cov} should be set to less than 6 mrad for sufficient site-selectivity, though a ϕ_{col} of 7.5 mrad for $NiFe_2O_4$ (Table. 1 & Fig. 3) still showed significant site-selectivity. Figure 4-c suggests that d should preferably be set to between 1 and 1.5 g, though one should seek an optimum value for d as a compromise between the signal intensity and site-selectivity, because the signal intensity is inversely proportional to $q^2q'^2$, as shown in Eq. (4).

Detector-position-sensitive ELCE

In the previous section, the EELS detector was located so as to keep the same boundary conditions for the incident and outgoing electrons. Recently, Saito *et al*. reported that the

incident beam focused on a particular site in a MgO crystal exhibited reversal Kikuchi band intensity distributions depending on the illuminated atomic column (Saito et al., 2010). This phenomenon was interpreted by the electron channeling effect using the reciprocity theorem. Inspired by this work, we propose and test an alternative experimental setup for ELCE: instead of consecutively tilting the incident beam direction with the detector position fixed with respect to the diffraction pattern, a position-sensitive two-dimensional detector (CCD) is placed with the spectral dispersion direction perpendicular to the operating *g*-vector, in a manner similar to position-sensitive EELS measurements (Reimer et al., 1992). Because the ELNES cross-section changes with the outgoing beam direction due to electron channeling along different atomic planes, detector-position-sensitive ELCE, in which each spectrum extracted from the row of the detector is derived from the outgoing wave on a different boundary condition corresponding to a different $\boldsymbol{k}_f$, is possible.

Figure 5 shows the theoretical dependence of the tetrahedral site signal fraction on the detector position for Fe-$L_{2,3}$ ELNES of $CoFe_2O_4$ at several incident convergence angles. In the calculation, the incident beam orientation is fixed at the exact Bragg condition of $\boldsymbol{g}$ = 400, w_{400} = 0 and ϕ_{col} = 0 (ideal detector). As expected, the fraction varies with the detector position, though more parallel illumination (smaller ϕ_{cov}) is required compared to the beam rocking method.

We attempted the corresponding experiment on Mn-$L_{2,3}$ ELNES of Mn_3O_4. The EELS

detector (100×1340 pixels^2 CCD) was set with the longer dimension (energy dispersion direction) aligned perpendicular to $\boldsymbol{g}$, as shown in Fig. 6-a. Because of the limited EELS entrance aperture size, subtending only ±0.5 g, the aperture position was subsequently displaced parallel to $\boldsymbol{g}$ to obtain the Mn $L_{2,3}$ spectra at three different aperture positions ranging from -1.5 to 1.5 $|\boldsymbol{g}_{400}|$, as shown in Fig. 6. The first and last 10 lines in the x-direction of the detector were not used, because the detector aperture is circular and the corresponding EELS derived from the edge regions collected much lower intensities. Ten adjacent spectra in the x-direction were averaged to reduce the statistical noise. Then, a total of 81×3 = 243 spectra were used for MCR analysis to extract the site-selective pure spectral components. Figure 6-b shows the theoretical distribution of the Mn $L_{2,3}$ signal intensity ratio of tetrahedral to octahedral sites in reciprocal space, simulating the detector position sensitivity and diffraction condition of Fig. 6-a. For simplicity, the calculation assumed both $\phi_{\mathrm{conv}} = 0$ and $\phi_{\mathrm{col}} = 0$. The experimental aperture positions shown in Fig. 6-a are indicated by the blue circles.

Two-component MCR analysis resolved the two pure spectral components (Fig. 7-a) and their relative fractions at each reciprocal position. The extracted relative fractions of the tetrahedral component were plotted as a function of the reciprocal coordinate in Fig. 7-b, together with the plot of theoretical $\sigma_{\mathrm{tet}}/(\sigma_{\mathrm{tet}} + N_{\mathrm{oct}}/N_{\mathrm{tet}}\ \sigma_{\mathrm{oct}})$, where the experimental ϕ_{conv} and detector size at each x were taken into account. The experimental relative tetrahedral signal fractions are qualitatively consistent with the theoretical ones, though the experimental profile

is asymmetric with respect to the reciprocal origin, unlike the symmetric theoretical profile. This is attributable to deteriorated specimen crystallinity by continuous electron illumination and/or deviation of the detector position from the ideal direction.

The resolved spectra corresponding to the tetrahedral and octahedral sites are compared with those calculated theoretically (Tatsumi et al., 2006) in Fig. 7-a. The experimental spectral profiles and the chemical shift of the L_3 main peak between the two sites are qualitatively consistent with the theoretical ones, confirming the known charge ordering of Mn_{tet}^{2+} and Mn_{oct}^{3+}. Hence, the detector-position-sensitive scheme does indeed work for site-dependent EELS analysis. For more precise measurements, the EELS collection aperture needs to be large enough to cover the entire reciprocal region of interest and preferably be rectangular. New-generation post-column energy filters allow this capability, and customization is in progress.

SUMMARY

We have investigated the site-selective ELCE, by combining experiment and theoretical calculation. The main results can be summarized as follows:

(1) The theoretical calculation scheme of ELNES cross-section was established for an arbitrary crystal orientation, incident beam convergence, EELS collection angle, and detector position. The present numerical calculation was confirmed to be consistent with the analytical

formula within the two-beam approximation for site-selective ELNES by the incident beam rocking method.

(2) Experimental site-specific ELCE measurements on three kinds of spinel ferrites with different measurement conditions were in reasonable agreement with the corresponding theoretical calculations on the basis of the present scheme.

(3) The optimum experimental parameters for the best site-selectivity were investigated through theoretical calculations. It was found that the beam convergence and detector collection semi-angles should preferably be less than 10 mrad for better site selectivity, while having a more parallel incident beam is more crucial. The optimum shift of the EELS entrance aperture from the optical axis was found to be between 1 and 1.5 g.

(4) A new experimental scheme for site-selective ELCE measurement was proposed instead of the conventional beam-rocking method, where the energy dispersion direction of the EELS CCD detector is aligned perpendicular to the operating g-vector. The feasibility of the proposed scheme was confirmed by both theoretical simulation and experiment on Mn_3O_4, where the fraction of site-specific components varied with respect to the detector CCD position, in agreement with the calculation. The extracted spectral profiles of the components were also consistent with theoretical first-principles results.

In conclusion, we would like to emphasize the significance of ELCE, which has often been criticized, by asking what is particularly superior about it to the current state-of-the-art

STEM-EELS system, which is capable of similar site-selective electronic structure measurements by atom column-by-column analysis using a sub-nanometer focused electron probe. ELCE offers the following advantages: (i) Atomic level column-by-column analysis requires precise alignment of the crystal orientation to a low-order zone axis, whereas a systematic row excitation condition is often sufficient for ELCE, which makes the method more flexible and widely applicable. (ii) Column-by-column analysis may also require utmost instrumental stability and may have to anticipate beam damage by the high density of focused electrons. These requirements are significantly relaxed for ELCE as long as the illuminated area is single crystalline. (iii) Compared to column-by-column analysis, ELCE favors thicker samples, which facilitates sample preparation. (iv) No aberration correction or field emission electron gun is necessary for ELCE. (v) ELCE and HARECXS can be performed simultaneously, which in principle provides quantitative information on both the site occupancies and chemical bonding states of the constituent elements. From the practical point of view, the present ELCE schemes could provide more robust results for quantitative analysis, although column-by-column analysis and ELCE can also complement each other, depending on the requirements, such as spatial resolution, quantification, types of materials of interest, instrumentation available, and so forth.

Acknowledgements

This work was supported in part by a Grant in Aid for Scientific Research of MEXT, Japan (Priority Area (#474) “Atomic Scale Modification”), JSPS (Wakate B: 21760516), the MST Foundation, and STINT.

References

ANTIC, B., KREMENOVIC, A., NIKOLIC, A.S. & STOILJKOVIC, M. (2004). Cation distribution and size-strain microstructure analysis in ultrarine Zn-Mn ferrites obtained from acetylacetonato complexes. *J. Phys. Chem.* B **108**, 12646-12651.

BATSON, P.E. (1993). Symmetry-selected electron-energy-eoss scattering in diamond. *Phys. Rev. Lett*. **70**, 1822-1825.

BLAHA, P., SCHWARZ, K., MADSEN, G.K.H., KVASNICKA, D. & LUITZ, J. (2001). *WIEN2K, An augmented plane wave + local orbitals program for calculating crystal properties*, Schwarz, K. TU Wien (Ed.), Austria, ISBN 3-9501031-1-2.

CALMELS, L. & RUSZ, J. (2011). Atomic site sensitivity of the energy loss magnetic chiral dichroic spectra of complex oxides. *J. Appl. Phys*. **109**, 07D328 (3 pp).

DENECKE, M.A., GUNSSNER, W., BUXBAUM, G. & KUSKE, P. (1992). Manganese valence in precipitated manganese ferrite. *Materials Research Bulletin* **27**, 507-514.

HETABA, W., LÖFFLER, S. & SHATTSCHNEIDER, P. (2011). Site specific elemental analysis using electron channeling In *Proceedings of the 10th Mutlinational Congress on Microscopy.* 53-54.

HETABA, W., LÖFFLER, S. & SHATTSCHNEIDER, P. (2012). Site-specific elemental analysis under electron channelling conditions. In *Proceedings of the 15th European Microscopy Congress*. (2 pp).

HIRSCH, P., HOWIE, A., NICHOLSON, R.B., PASHLEY, D.W. & WHELAN, M.J. (1977). *Electron Microscopy of Thin Crystals*, Chap. 8, London: Butterworths.

HOLGERSSON, S., (1927). Roentgenographische Strukturuntersuchungen der Mineralien der Spinellgruppe und von synthetisch dargestellten Substanzen vom Spinelltyp. *Lunds universitets årsskrift. N.F. Avd. 2.* **23**, 1-9.

KOHL, H. & ROSE, H. (1985). Theory of image-formation by inelastically scattered electrons in the electron-microscope. *Advances in Electronics and Electron Optics* **65**, 173-226.

KRIVANEK, O.L., DISKO, M.M., TAFTØ, J. & SPENCE, J.C.H. (1982). Electron energy loss spectroscopy as a probe of the local atomic environment. *Ultramicroscopy* **9**, 249-254.

MASLEN, V.W. & ROSSOUW, C.J. (1984). Implications of (e,2e) scattering for inelastic electron-diffraction in crystals. 1. theoretical. *Phil. Mag.* A **49**, 735-742.

MATSUMURA, S., SOEDA, T., ZALUZEC, N.J. & KINOSHITA, C. (1999). Electron channeling x-ray microanalysis for cation configuration in irradiated magnesium aluminate spinel. In *MRS Meeting Proc.* **589**, 129.

NELHIEBEL, M., SCHATTSCHNEIDER, P. & JOUFFREY, B. (2000). Observation of ionization in a crystal interferometer. *Phys. Rev. Lett.* **85**, 1847-1850.

NESVIZHSKII, A.I., ANKUDINOV, A.L. & REHR, J.J. (2001). Normalization and

convergence of x-ray absorption sum rules. *Phys. Rev.* B **63**, 094412 (5 pp). Although we do not consider the multiplet splitting, it would not change the EELS site-selection significantly, because the splitting is a few eV and much smaller than the integration energy range.

OXLEY, M.P. & ALLEN, L.J. (2003). ICSC: a program for calculating inelastic scattering cross sections for fast electrons incident on crystals. J. Appl. Cryst. **36**, 940-943.

REIMER, L., FROMM, I., HIRSCH, P., PLATE, U. & RCNNEKAMP, R. (1992). Combination of EELS modes and electron spectroscopic imaging and diffraction in an energy-filtering electron microscope. *Ultramicroscopy* **46**, 335-347.

ROSSOUW, C.J. & MASLEN, V.W. (1984). Implications of (e,2e) scattering for inelastic electron-diffraction in crystals. 2. application of the theory. *Phil. Mag.* A **49**, 743-757.

RUSZ, J., RUBINO, S. & SCHATTSCHNEIDER, P. (2007). First-principles theory of chiral dichroism in electron microscopy applied to 3*d* ferromagnets. *Phys. Rev.* B **75**, 214425 (9 pp).

RUSZ, J., MUTO, S. & TATSUMI, K. (2013). New algorithm for efficient Bloch-waves calculations of orientation-sensitive ELNES. *Ultramicroscopy* **125**, 81-88.

SAITOH, K., TATARA, Y. & TANAKA, N. (2010). Atom-column distinction by Kikuchi pattern observed by an aberration-corrected convergent electron probe. *J. Electron Microscopy* **59**, 387-394.

SALDIN, D.K. (1987). The theory of electron energy-loss near-edge structure. *Phil. Mag.* B **56**, 515-525.

SCHATTSCHNEIDER, P., NELHIEBEL, M., SCHENNER, M., GROGGER, W. & HOFFER, F. (1996). Diffraction effects in inner-shell ionization edges. *J. Microsc.* **183**, 18-26.

SCHATTSCHNEIDER, P., JOUFFREY, B. & NELHIEBEL, M. (1996). Dynamical diffraction in electron-energy-loss spectrometry: The independent Bloch-wave model. *Phys. Rev.* B **54**, 3861-3868.

SCHATTSCHNEIDER, P., HÉBERT, C. & JOUFFREY, B. (2001). Orientation dependence of ionization edges in EELS. *Ultramicroscopy* **86**, 343-353.

SCHATTSCHNEIDER, P., RUBINO, S., HÉBERT, C., RUSZ, J., KUNEŠ, J., NOVÁK, P., CARLINO, E., FABRIZIOLI, M., PANACCIONE, G. & ROSSI, G. (2006). Detection of magnetic circular dichroism using a transmission electron microscope. *Nature* (London), **441**, 486-488.

SCHATTSCHNEIDER, P. (1986). *Fundamentals of Inelastic Electron Scattering*. Wien: Springer.

SPENCE, J.C.H. & ZUO, J.M. (1992). *Electron Microdiffraction*. New York: Plenum Press.

SPENCE, J.C.H. & TAFTØ, J. (1983). ALCHEMI - a new technique for locating atoms in small crystals. *J. Microsc.* **130**, 147-154

TAFTØ, J. & KRIVANEK, O.L. (1982). Site-specific valence determination by electron

energy-loss spectroscopy. *Phys. Rev. Lett.* **48**, 560-563.

TAFTØ, J. & KRIVANEK, O.L. (1982). Characteristic energy losses from channeled 100 keV electrons. *Nucl. Inst. Meth.* **194**, 153-158.

TAFTØ, J. (1987). Reciprocity in electron energy-loss spectra from non-centrosymmetric crystals. *Acta Cryst*. **A43**, 208-211.

TATSUMI, K. & MUTO, S. (2009). Local electronic structure analysis by site-selective ELNES using electron channeling and first-principles calculations. *J. Phys.:Condens. Matter* **21**, 104213 (14 pp).

TATSUMI, K., MUTO, S., YAMAMOTO, Y., IKENO, H., YOSHIOKA, S. & TANAKA I. (2006). Site-specific electronic structure analysis by channeling EELS and first-principles calculations. Ultramicroscopy **106**, 1019-1023.

TATSUMI, K., MUTO, S., NISHIDA, I. & RUSZ, J. (2010). Site-specific electronic configurations of Fe 3*d* states by energy loss by channeled electrons. *Appl. Phys. Lett.*, **96** 201911 (3 pp).

WANG, Z.Q., ZHONG, X.Y., YU., R, CHENG, Z.Y. & ZHU, J. (2013). Quantitative experimental determination of site-specific magnetic structures by transmitted electrons. *Nature Comm.* **4** 1395 (5 pp).

WEICKENMEIER, A. & KOHL, H. (1989). Computation of the atomic inner-shell excitation cross-sections for fast electrons in crystals. *Phil. Mag.* B **60**, 467-479.

WEICKENMEIER, A. & KOHL, H. (1991). Computation of absorptive form factors for high-energy electron diffraction. *Acta Crystallogr*., *Sect. A: Found. Crystallogr.* **A47**, 590-597.

YAMAMOTO, Y., TATSUMI, K. & MUTO, S. (2007). Site-selective electronic structure of aluminum in oxide ceramics obtained by tem-eels analysis using the electron standing-wave method. *Mater. Trans.* **48**, 2590-2594.

ZALUZEC, N.J., BLACKFORD, M.G., SMITH, K.L. & COLELLA, M. (2005). HARECES Measurements of Carbon K Shell Excitation in Graphite. *Microsc. Microanal.* **11**, S2 718-719.

Figure Legends

Fig. 1 Comparison between tetrahedral signal fractions of Fe $L_{2,3}$ ELNES in $NiFe_2O_4$ spinel calculated from MDFFs by the electric dipole approximation (Eq. (5)) (open squares) and by the full first-principles electronic structure (filled squares) as functions of the incident beam orientation. The inset shows the diffraction geometry of direct and excited diffraction spots ($\boldsymbol{g}$ = 400) and EELS aperture position with $|\boldsymbol{d}|$=1.0 g. For simplicity, the calculations are done for the parallel beam (ϕ_{conv} = 0) and ideal detector (ϕ_{col} = 0).

Fig. 2 Comparison between numerically and analytically calculated curves for site-selectivity in Al-K ELNES of $NiAl_2O_4$, under the two-beam approximation without (a) and with (b) phenomenological absorption through the imaginary part of the extinction distance. The calculations were done for the same geometry as in the inset of Fig. 1.

Fig. 3 Comparison of the tetrahedral site signal fraction in Fe $L_{2,3}$ ELNES of three spinel ferrites between numerical calculation and experiment (a). The relative Fe occupancy parameter, N_{oct}/N_{tet}, was included. Comparison between theoretical and experimental profiles of normalized site-specific cross-section ratios (b). See text for details.

Fig. 4 Theoretical tetrahedral signal fractions on Fe-$L_{2,3}$ of $CoFe_2O_4$ for five different

collection semi-angles ϕ_{col} in mrad (top), convergent semi-angles ϕ_{cov} in mrad (middle) and EELS entrance aperture off-axis shift d in g (bottom) for the instrumental setup shown in the inset of Fig. 1.

Fig. 5 Theoretical simulation of site-selective ELCE using a position-sensitive EELS detector. The dispersion direction of the detector is aligned perpendicular to the x-direction. Instead of rocking the incident beam direction, the respective arrays along the dispersion at different x coordinates collect differently channeled outgoing electrons, with the diffraction condition fixed.

Fig. 6 Experimental (025) diffraction pattern (DP) of spinel Mn_3O_4 (6-a), showing the detector positions for position-sensitive ELCE, with the $\boldsymbol{g}$ = 400 systematic row symmetrically excited. Two-dimensional map of theoretical relative ratio of site-specific ELNES cross-sections (6-b), with respect to the EELS detector position projected onto the DP. The blue circles denote the three EELS aperture positions used in the experiment.

Fig. 7 Comparison between experiment and theory for the Mn $L_{2,3}$ site-specific spectra (7-a) and for the tetrahedral site signal fractions with respect to the EELS detector position (7-b).

Table 1 List of experimental parameters used for t three types of spinel ferrites.

	$CoFe_2O_4$	**$MnFe_2O_4$**	**$NiFe_2O_4$**
Convergent semi-angle, ϕ_{conv} (mrad)	11.0	4.9	4.6
Collection semi-angle, ϕ_{col} (mrad)	3.8	7.5	7.5
Aperture off-axis shift ($1/g_{400}$)	1.0	2.0	1.5

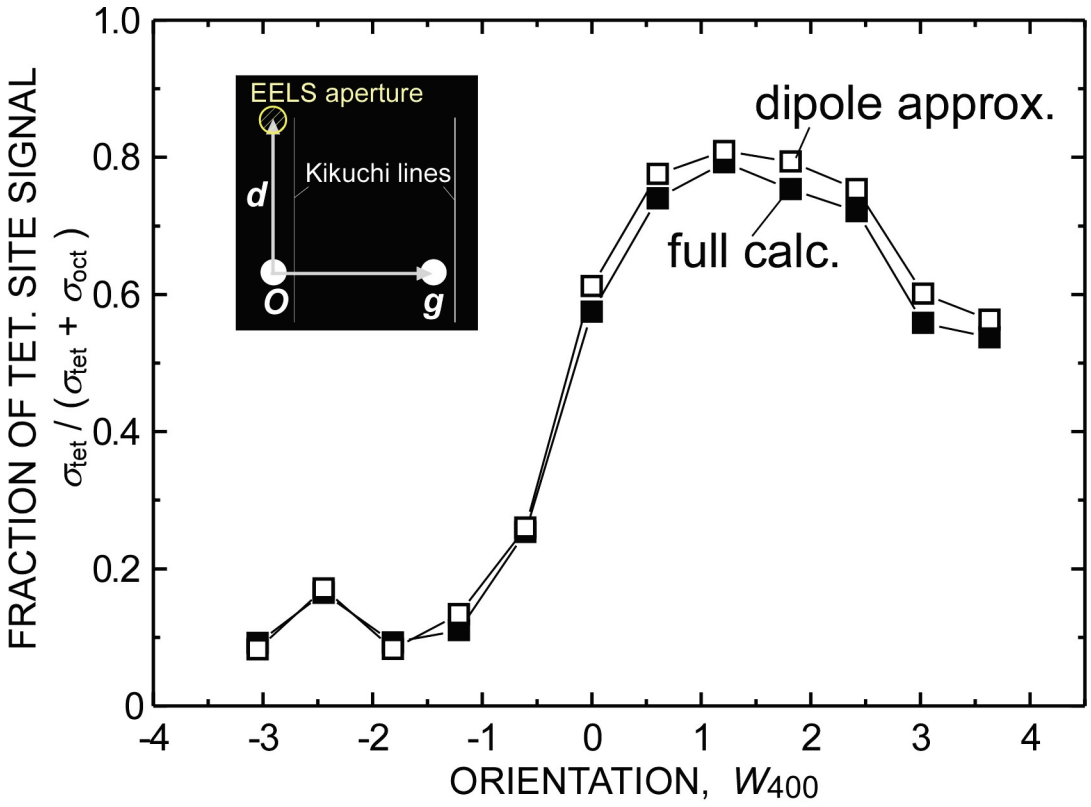

Fig.1 dipole vs full calc (wien2k)

Fig. 1 Comparison between tetrahedral signal fractions of Fe $L_{2,3}$ ELNES in $NiFe_2O_4$ spinel calculated from MDFFs by the electric dipole approximation (eq. (5)) (open square) and by the full first principles electronic structure (filled square) as functions of the incident beam orientation. The inset shows the diffraction geometry of direct and excited diffraction spots ($\boldsymbol{g}$=400) and EELS aperture position with |**d**|=1.0 g. The calculations are done for the parallel beam (ϕ_{conv} = 0) and ideal detector (ϕ_{col} = 0) for simplicity.

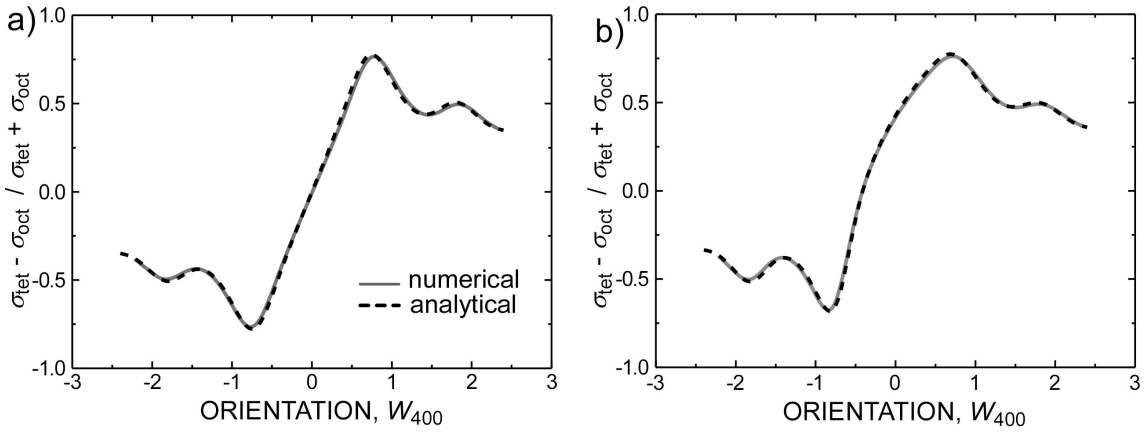

Fig. 2 K. Tatsumi *et al*.

Fig. 2 Comparison between numerically and analytically calculated curves for the site-selectivity in Fe-$L_{2,3}$ ELNES of $NiFe_2O_4$, under the two-beam approximation without (a) and with (b) the phenomenological absorption through the imaginary part of the extinction distance. The calculations were done at the same geometry as inset of Fig. 1.

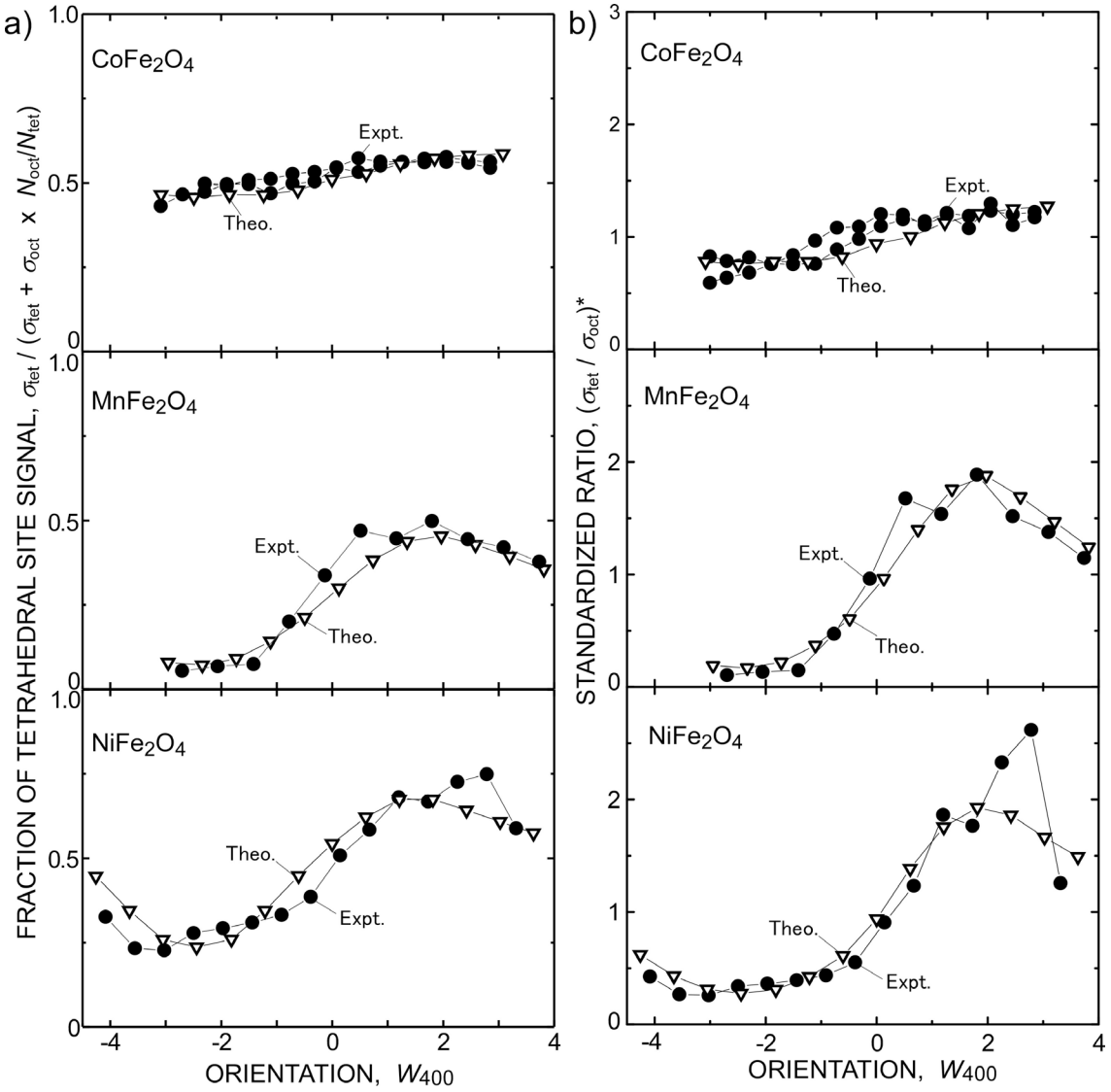

Fig. 3 Comparison of the tetrahedral site signal fraction in Fe $L_{2,3}$ ELNES of the three spinel ferrites between numerical calculation and experiment (a). The relative Fe occupancy parameter, N_{oct}/N_{tet}, was included. Comparison between theoretical and experimental profiles of the normalized site-specific cross section ratios (b). See text for detail.

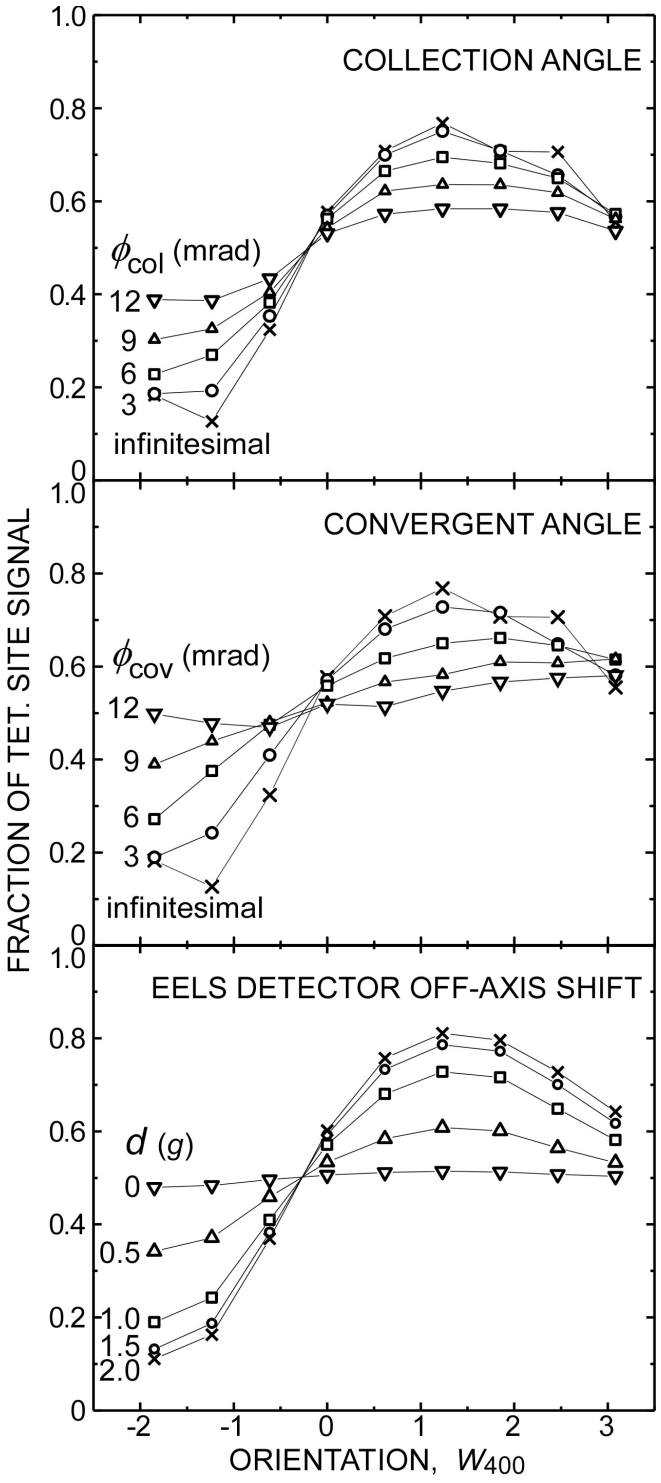

Fig. 4 K. Tatsumi *et al.*

Fig.4 Theoretical tetrahedral signal fractions for five different collection semi-angles ϕ_{col} in mrad (top), convergent semi-angles ϕ_{cov} in mrad (middle) and EELS entrance aperture off-axis shift d in g (bottom) in the instrumental geometry inset of Fig.1.

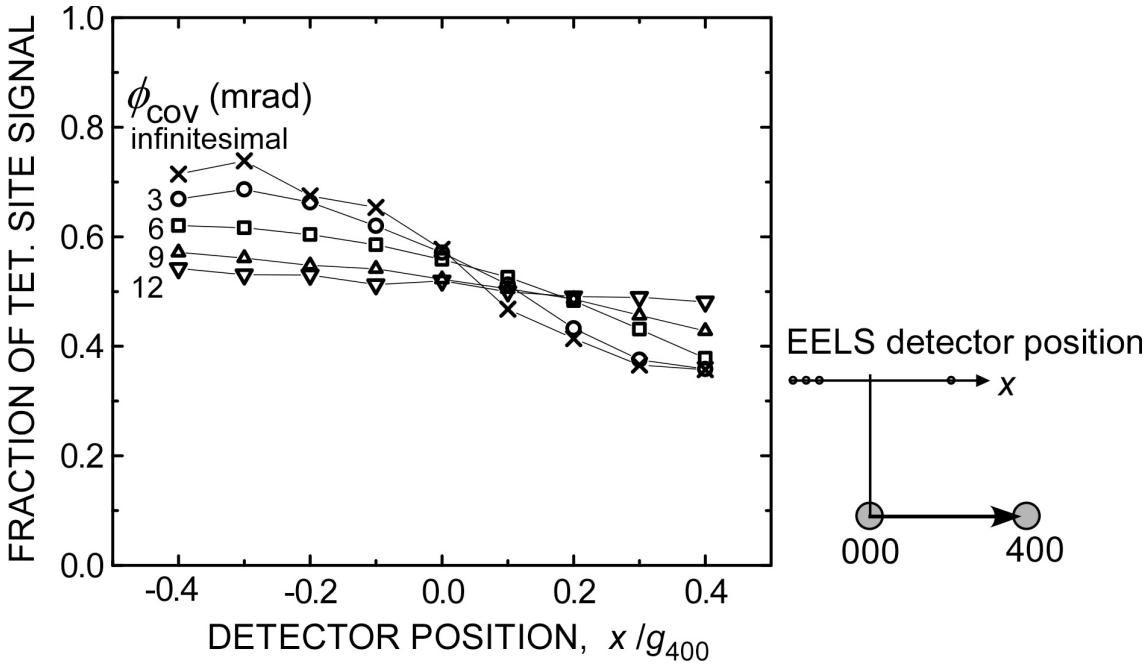

Fig.5 K. Tatsumi *et al*.

Fig. 5 Theoretical simulation of site-selective ELCE using position sensitive EELS detector. The dispersion direction of the detector is placed perpendicular to the *x*-direction. Instead of rocking the incident beam direction, the respective arrays along the dispersion at different *x* coordinates collect differently channeled outgoing electrons with the diffraction condition fixed.

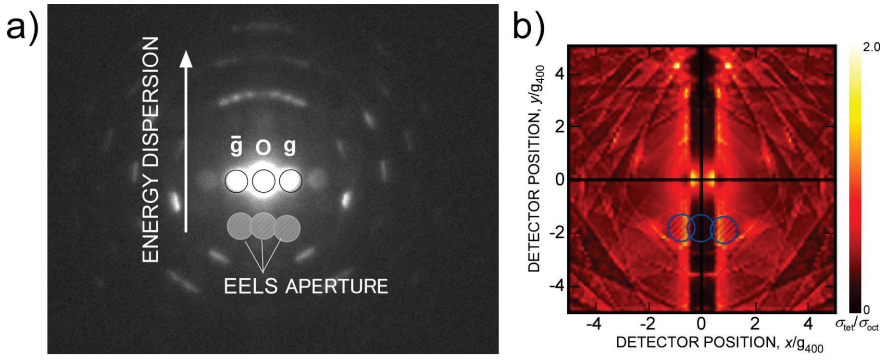

Fig.6 K. Tatsumi *et al*.

Fig. 6 experimental (025) diffraction pattern (DP) of spinel Mn_3O_4 (6-a), showing the detector positions for position sensitive ELCE, with the ***g***=400 systematic row symmetrically excited. Two-dimensional map of theoretical relative ratio of site-specific ELNES cross sections (6-b), with respect to the EELS detector position projected onto the DP. The blue circles denote the three EELS aperture positions in the experiment.

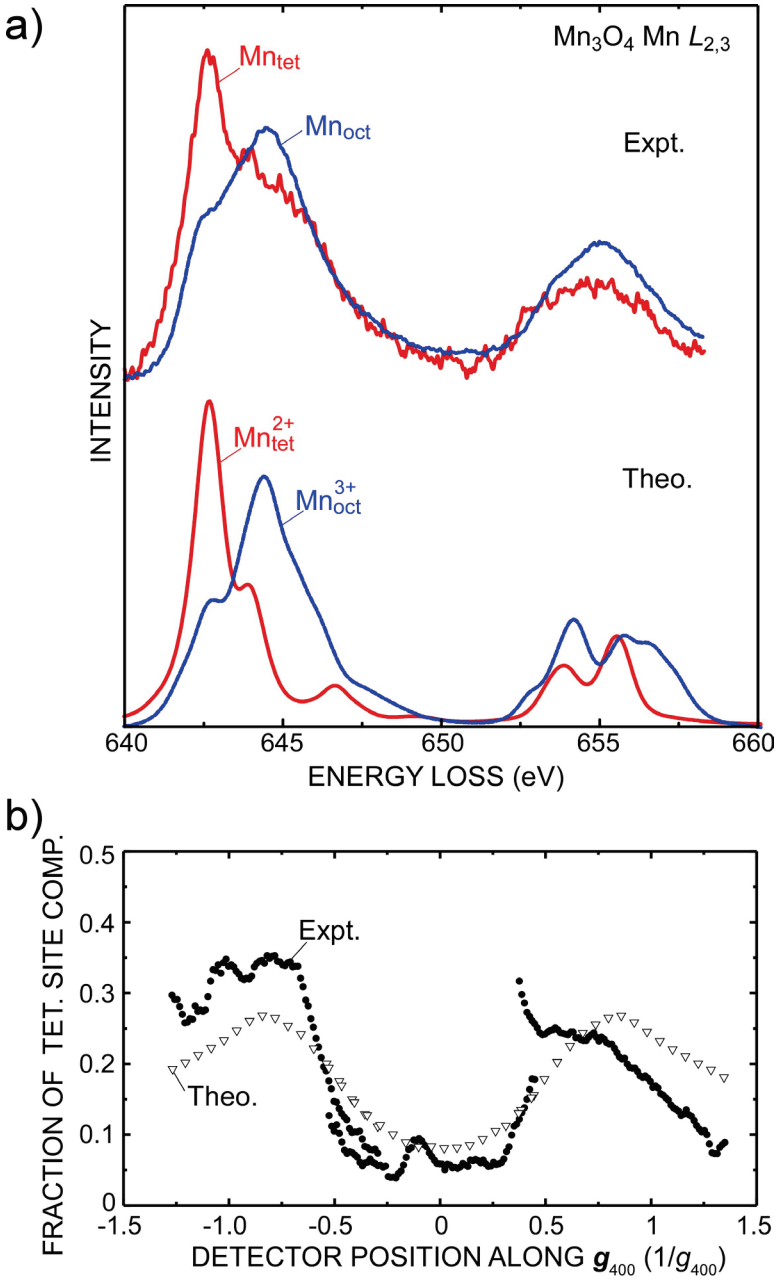

Fig.7 K. Tatsumi *et al.*

Fig. 7 Comparison between experiment and theory for the Mn $L_{2,3}$ site-specific spectra (7-a) and for the tetrahedral site signal fractions with respect to the EELS detector position (7-b).